npj | clean water

Article

Published in partnership with King Fahd University of Petroleum & Minerals

https://doi.org/10.1038/s41545-025-00476-0

Fe^{III}-driven self-cycled Fenton via contact-electro-catalysis for water purification

Check for updates

Dongmei Ma[1,2,5], Jin Zhang[1,5], Wei Li[1,2] ✉, Jinxing Ma[3], Kuanchang He[3], Kui Yang[3], Jianghu Cui[1,2], Qian Liu[1], Sihao Lv[1], Min Zhang[2], Faliang Cheng[2] & Defeng Xing[4]

While self-cycled Fenton (SC-Fenton) systems represent an innovative advancement in water purification technologies, their practical implementation remains constrained by inefficient in situ H_2O_2 generation. To address this limitation, we developed a mechano-driven contact-electro-catalysis (CEC) platform employing fluorinated ethylene propylene (FEP) as a triboelectric catalyst. Under ultrasound irradiation, this system achieves an exceptional H_2O_2 generation rate of 7.67 mmol·g_{cat}^{-1}·h^{-1}, outperforming conventional piezo-catalysis systems. Mechanistic studies reveal that a built interfacial electric field generated on the FEP surface effectively reduces the free energy for the indirect $2e^-$ water oxidation pathway. This unique characteristic promotes the generation of interfacial hydroxyl radical ($^*OH$) and enhances its subsequent recombination into H_2O_2. The strategic integration of Fe^{III} as a catalytic initiator with the CEC system enables the establishment of SC-Fenton reaction (Fe^{III}/FEP/CEC). Notably, the contact-electrification electrons accumulated on the FEP interface drive efficient Fe^{III}/Fe^{II} redox cycling, achieving a remarkable degradation rate for sulfadiazine at 0.125 min^{-1}. This enhanced catalytic performance stems from Fe^{III}-mediated amplification of dissociative hydroxyl radical ($^\bullet OH$) generation. This study provides fundamental insights into the underlying mechanisms of CEC-mediated Fe^{III}-initiated SC-Fenton reaction, offering new possibilities for sustainable water purification processes.

Fenton technology is widely recognized as a well-established method for wastewater remediation, leveraging reactive oxygen species (ROS) generated through the catalytic interplay between hydrogen peroxide (H_2O_2) and Fe^{II} to degrade pollutants[1]. However, persistent challenges including continuous H_2O_2 consumption and sluggish Fe^{II} regeneration from Fe^{III} reduction have constrained the advancement of conventional Fenton processes[2–4]. To address these limitations, the concept of self-cycled Fenton (SC-Fenton) systems has emerged, designed to concurrently regenerate Fe^{II} and synthesize H_2O_2 within an integrated redox framework. These closed-loop systems enable sustained pollutant degradation while minimizing reagent replenishment, attracting considerable research interest in sustainable water treatment[5]. Early implementations of SC-Fenton systems primarily integrated photocatalytic or piezocatalytic mechanisms with Fe^{III} activation[6,7]. Theses hybrid architectures leverage photo/piezocatalytic effects to achieve charge carrier (electron (e^-) and hole (h^+)) separation, wherein the generated e^- concurrently participate in two critical processes: (1) oxygen reduction to H_2O_2 (ORR-H_2O_2, Eqs. 1), and (2) Fe^{III} reduction to Fe^{II}. The regenerated Fe^{II} subsequently reacts with in situ formed H_2O_2 to perpetuate the Fenton cycle[8,9]. However, such configurations suffer from two inherent limitations that constrain catalytic efficiency: First, competitive e^- consumption between ORR-H_2O_2 and Fe^{III} reduction creates a kinetic bottleneck, diminishing the availability of e^- for either pathway. Second, the ORR-H_2O_2 process exhibits intrinsically low yield due to limited dissolved oxygen concentrations in wastewater matrices, imposing fundamental constraints on system scalability[10]. These interdependent challenges–e^- pathway competition and oxygen-dependent H_2O_2 synthesis–collectively restrict the performance of Fe^{III}-mediated photo/piezocatalysis-driven SC-Fenton (Fig. 1a).

The water oxidation reaction (WOR-H_2O_2) has emerged as a promising alternative pathway for H_2O_2 production, offering distinct advantages over ORR-H_2O_2. First, WOR-H_2O_2 utilizes ubiquitous H_2O as the H and O source while circumventing the oxygen-dependent constraints

[1]Research Center for Eco-environmental Engineering, School of Environment and Civil Engineering, Dongguan University of Technology, Dongguan, 523808, China. [2]Guangdong Engineering and Technology Research Center for Advanced Nanomaterials, School of Environment and Civil Engineering, Dongguan University of Technology, Dongguan, 523808, China. [3]School of Ecology, Environment and Resources, Guangdong University of Technology, Guangzhou, 510006, China. [4]State Key Laboratory of Urban Water Resource and Environment, School of Environment, Harbin Institute of Technology, Harbin, 150090, China. [5]These authors contributed equally: Dongmei Ma, Jin Zhang. ✉e-mail: liwei@dgut.edu.cn

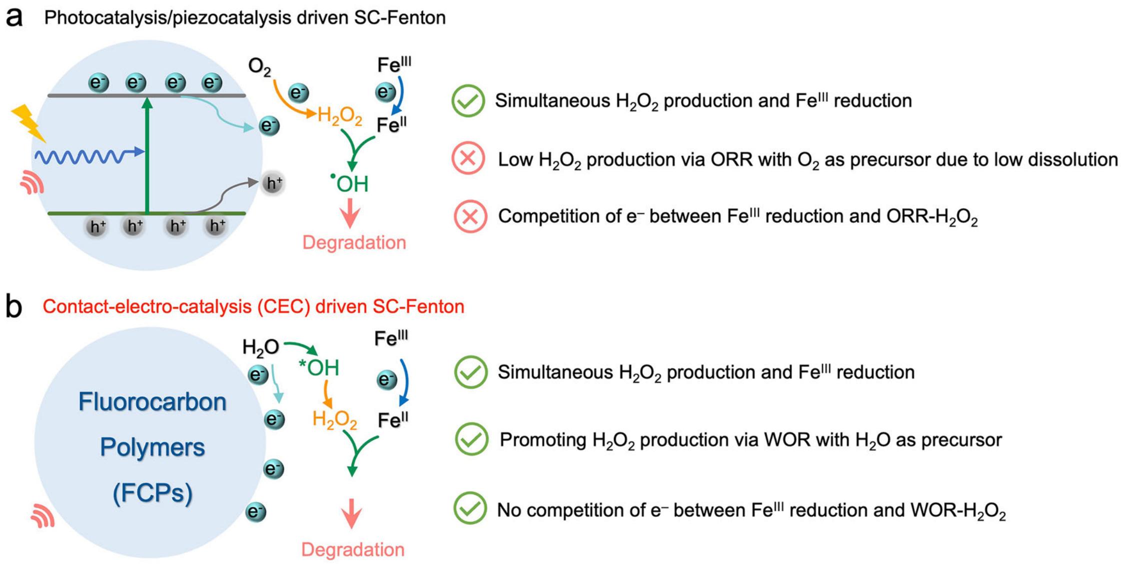

Fig. 1 | Contact-electro-catalysis with Fe^{III}-based self-cycled Fenton system: comparison and improvements. The principle and challenges of Fe^{III}-based photocatalysis/piezocatalysis-driven SC-Fenton system (**a**). The princple and improvements of Fe^{III}-based CEC-driven SC-Fenton (**b**).

inherent to ORR-H_2O_2[11,12]. Second, this oxidative pathway operates through hole (h^+)-mediated oxidation processes, thereby eliminating e^- competition with parallel Fe^{III} reduction reactions[13,14]. Third, Fe^{III} reduction and WOR reactions exhibit synergistic interdependency, mutually enhancing reaction kinetics[15]. However, compared to the dominant 4e^- WOR pathway for O_2 evolution (Eq. 2), the 2e^- WOR pathway (direct/indirect routes; Eqs. 3–5) requires a higher thermodynamic overpotential, imposing significant energy barriers for most catalytic systems[16,17]. This energy penalty currently limits H_2O_2 yield via the 2e^- WOR process, underscoring the need for advanced catalyst engineering to optimize reaction energetics.

2e^- ORR

$$O_2 + 2H^+ + 2e^- \rightarrow H_2O_2 \quad 0.69\ \mathrm{V\ vs.\ NHE} \tag{1}$$

4e^- WOR

$$2H_2O + 4h^+ \rightarrow O_2 + 4H^+ \quad 1.23\ \mathrm{V\ vs.\ NHE} \tag{2}$$

Direct 2e^- WOR

$$2H_2O + 2h^+ \rightarrow H_2O_2 \quad 1.76\ \mathrm{V\ vs.\ NHE} \tag{3}$$

Indirect 2e^- WOR

$$H_2O + h^+ \rightarrow {*OH} \quad 2.73\ \mathrm{V\ vs.\ NHE} \tag{4}$$

$$2{*OH} \rightarrow H_2O_2 \tag{5}$$

Overcoming the energy barrier of the 2e^- WOR could unlock the full potential of WOR-H_2O_2 for the SC-Fenton system[18]. Recent advances highlight in situ formed interfacial electric field (IEF) as transformative tools for modulating reaction energetics. For example, in a piezo-photocatalysis system, non-centrosymmetric semiconductors generate IEF via mechanical stress, which lowers the activation energy for 2e^- WOR through lattice polarization[18]. Analogously, the contact-electrification (CE) effect within the contact-electro-catalysis (CEC) system leverages solid-liquid CE to establish IEF at interfaces. During solid-liquid interactions, the electron transfer driven by electron clouds overlapping creates electron accumulation on fluorocarbon polymers (FCPs)[19]. These accumulated electrons establish intense built-in IEF (up to ~100 V) that dissociate interfacial water molecules into hydrated electrons and interfacial hydroxyl radical (*OH), followed by *OH recombination into H_2O_2[20–22]. While prior studies confirm CEC's capacity for H_2O_2 accumulation[23,24], critical knowledge gaps persist regarding: (i) thermodynamic optimization of H_2O decomposition and *OH recombination; and (ii) charge transfer dynamics at interfaces. Charged FCPs exhibit unique charge reservoir behavior, where surface-trapped electrons facilitate cation reduction under IEF guidance[25–27]. These properties suggests that the CEC system exhibits dual functional advantages for Fe^{III}-based SC-Fenton applications (Fig. 1b): (i) concurrent facilitation of Fe^{III} reduction and WOR-H_2O_2 through distinct e^- transfer pathway, effectively eliminating inter-pathway e^- competition; and (ii) enhanced H_2O_2 production efficiency via IEF-optimized WOR-H_2O_2 mechanisms. This functional synergy addresses two critical limitations of conventional systems by decoupling oxidative and reductive processes while amplifying H_2O_2 yield. To fully elucidate the underlying mechanisms, three fundamental questions require systematic resolution: (i) the interfacial electron transfer dynamics governing Fe^{III}/Fe^{II} conversion; (ii) IFE-mediated radical generation efficiency; and (iii) kinetic coupling mechanisms between oxidative (H_2O_2 accumulation) and reductive (Fe^{II} regeneration) processes.

In this study, a high-performance SC-Fenton system was developed, which synergized FCPs-based CEC (FCPs/CEC) with homogeneous Fe^{III} activation. The FCPs/CEC platform achieved an exceptional H_2O_2 generation rate of 7.67 $\mathrm{mmol \cdot g_{cat}^{-1} \cdot h^{-1}}$ through IEF-mediated indirect 2e^- WOR, where the IEF reduced the thermodynamic barrier for *OH formation and subsequent H_2O_2 generation. Upon Fe^{III} integration, the resulting SC-Fenton system (Fe^{III}/FCPs/CEC) exhibited amplified generation of dissociative hydroxyl radical (•OH) via Fenton chain reactions, leading to improved pollutant degradation kinetics compared to both FCPs/CEC and Fe^{II}/FCPs/CEC systems. In addition, the catalytic degradation capability of the Fe^{III}/FCPs/CEC remained robust during reuse and in complex water matrices. This study provides fundamental insights into the CEC-enabled SC-Fenton paradigm, demonstrating how triboelectric fields can concurrently address H_2O_2 synthesis and Fe^{III} activation bottlenecks.

Results

Efficient H_2O_2 generation of FCPs/CEC

The contact-electro-catalytic activity of FCPs/CEC for H_2O_2 generation was assessed under ultrasound irradiation (40 kHz, 110 W) of DI water with different FCPs at a dosage of 0.1 $\mathrm{g \cdot L^{-1}}$. The H_2O_2 concentration was quantitatively calculated by the standard curve in Supplementary Fig. 1. Figure 2a illustrated that the accumulated H_2O_2 yield was 0.76, 0.54, and 0.03 mM for FEP, PTFE, and PVDF/CEC within 60 min, respectively, with

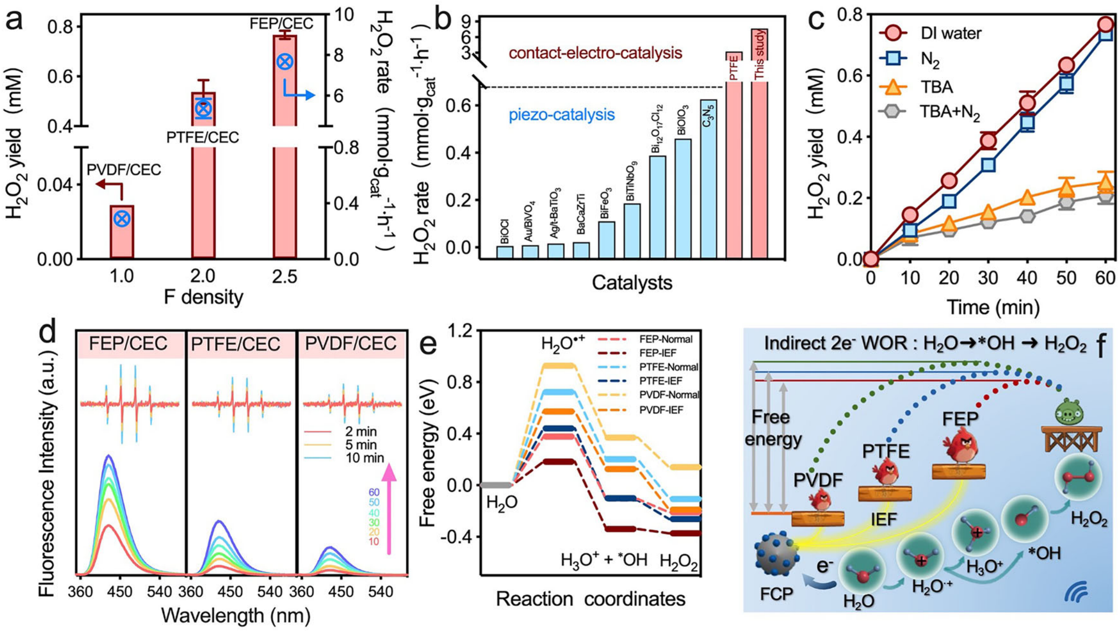

Fig. 2 | Investigation into the mechanism of H_2O_2 generation by FCPs/CEC. Time course of the H_2O_2 generation by FCP/CEC with different FCPs (**a**). Comparison of the H_2O_2 generation rate with previous CEC and piezo-catalysis (**b**). Time course of the H_2O_2 generation measured under different reaction conditions (**c**). Relative quantitative analysis of $^*OH$ in FCP/CEC (**d**). Free energy profiles of the indirect 2e$^-$ WOR process in FCP/CEC were compared with (FCP-IEF) and without IEF (FCP-Normal) (**e**). Schemic of H_2O_2 generation in FCPs/CEC (**f**). Experimental conditions: $[FCPs]_0 = 0.1\ g{\cdot}L^{-1}$, T = 25 ± 2 °C.

all of their generation rates adhering to zero-order kinetics. Evidently, the H_2O_2 generation was driven by the FCPs/CEC process, as negligible H_2O_2 accumulation was observed without the introduction of FCPs (Supplementary Fig. 2). Remarkably, H_2O_2 accumulation showed a direct positive correlation with –F density (F/C atomic ratio on the main chain) across FCPs (Supplementary Table 1 and Supplementary Fig. 3a), establishing –F density as a critical factor governing CE capacity through enhanced electron transfer efficiency and reduced activation barriers in FCPs/CEC systems[28]. Moreover, quantitative characterization of interfacial electron transfer revealed distinct CE capabilities: FEP demonstrated superior charge accumulation (20.3 nC), followed by PTFE (13.7 nC) and PVDF (2.7 nC) during aqueous contact (Supplementary Fig. 3b). Consistent with this trend, CE performance showed F-dependent enhancement (Supplementary Fig. 3c), conclusively demonstrating that –F density dictates electron-withdrawing capacity in FCP architectures. This implied that utilizing FCPs with higher CE ability enhanced H_2O_2 generation in FCPs/CEC, with FEP currently being identified as the optimal CEC catalyst for this purpose. Therefore, in this investigation, FEP/CEC demonstrated an exceptional normalized H_2O_2 generation rate of 7.67 $mmol{\cdot}g_{cat}^{-1}{\cdot}h^{-1}$, surpassing the performance of cutting-edge particle H_2O_2 catalysts by 2–126 times (Fig. 2b and Supplementary Table 2), including C_3N_5, $Bi_{12}O_{17}Cl_{12}$, and $BiOIO_3$, etc. in the piezo-catalysis systems[9,15,29–35].

To elucidate the mechanisms behind the remarkable rate of H_2O_2 generation in FCPs/CEC, the potential ORR and WOR processes were examined individually[36]. This investigation began by exploring the H_2O_2 yield under ambient and anoxic aqueous conditions. The results, as depicted in Fig. 2c, revealed a slight decrease in H_2O_2 production when dissolved oxygen was expelled by N_2, indicating that the 2e$^-$ ORR pathway made only a modest contribution to H_2O_2 generation in FCPs/CEC. These results suggested that the primary pathway for H_2O_2 generation in FCPs/CEC was the WOR process. Subsequently, the specific types of WOR reactions were further elucidated. One established method to differentiate between direct and indirect 2e$^-$ WOR processes is by detecting intermediated $^*OH$[18]. Notably, a significant reduction in H_2O_2 generation (only 0.25 mM) was observed upon the addition of *tert*-butyl alcohol (TBA, 200 mM) as the scavenger of $^*OH$ (Fig. 2c), indicating the pivotal role of intermediated $^*OH$ in the evolution of H_2O_2 in FCPs/CEC[18]. Moreover, the presence of the quadruplet DMPO-$^*OH$ signals and fluorescent peaks in Fig. 2d confirmed the generation of $^*OH$ in FCPs/CEC. The intensity of both electron paramagnetic resonance (EPR) signals and fluorescent peaks correlated with the accumulated H_2O_2 yield in the order of FEP > PTFE > PVDF, suggesting that the generation of $^*OH$ was ascribed to induced electron exchanges between the FCP-H_2O interface during frequent contact/separation. These results pointed towards the indirect 2e$^-$ WOR process as the primary pathway for H_2O_2 evolution.

The intricate pathway underlying the indirect 2e$^-$ WOR process for H_2O_2 generation in FCPs/CEC was unveiled through meticulous DFT calculations (without and with IEF), shedding light on the activation energy dynamics. The interfacial interaction between FCPs and H_2O constitutes the fundamental initiation step of CEC. To quantify this critical interfacial process, we systematically calculated adsorption energies for FCP–H_2O systems. As shown in Supplementary Table 3, FEP exhibited the highest H_2O adsorption affinity among the evaluated FCPs, a phenomenon directly attributable to its superior electron-withdrawing capacity derived from higher –F density. This computational assessment reveals that enhanced electron-withdrawing characteristics in FCPs significantly facilitate interfacial charge transfer processes by strengthening molecular-level interactions at the FCP–H_2O interface. The observed hierarchy in adsorption energy aligns precisely with the FCPs' –F density and corresponding electronic properties, establishing a quantitative structure-activity relationship central to CEC modulation. Furthermore, computational models incorporating 7 H_2O molecules were employed to simulate FCP–H_2O interfacial interactions, with a superimposed 0.3 V/Å IEF replicating localized high-intensity electrochemical conditions (Fig. 2e and Supplementary Fig. 4). Comparative analysis revealed a pronounced IEF catalytic effect: the activation energies for $^*OH$ generation substantially decreased across systems–from 0.37 to 0.18 eV (FEP/CEC), 0.72 to 0.44 eV (PTFE/CEC), and 0.92 to 0.57 eV (PVDF/CEC)–indicating enhanced thermodynamic preference for the indirect 2e$^-$ WOR pathway under IEF, thereby promoting H_2O_2 accumulation. Non-bonding interaction at the FCP–H_2O interface facilitated unimpeded diffusion of both H_2O molecules and intermediated $^*OH$ around FEP, increasing interfacial contact frequency and subsequent $^*OH$ recombination[37]. Notably, the inverse correlation between activation energy hierarchy (FEP < PTFE < PVDF) and CE capacity arose from

F-mediated electron accumulation–FCPs with superior CE ability exhibited amplified surface electron density due to strong electron-withdrawing –F groups (Supplementary Fig. 3), which intensified IEF strength and consequently reduced energy barriers for indirect $2e^-$ WOR pathway[38]. Although the piezo-effect could induce an IEF under ultrasound, the induced IEF was comparably weaker than that of CEC, as evidenced by the lower output voltage of piezoelectric nanogenerators (~3.2 V) in contrast to triboelectric nanogenerators (~130 V)[39–41]. This discrepancy highlighted the increased difficulty and reaction barriers in radical formation during piezo-catalysis compared to CEC. Alternatively, the higher energy barrier toward indirect $2e^-$ WOR was needed to be overcome for piezo-catalysis than that of CEC, which exactly explained that the indirect $2e^-$ WOR cannot be achieved by piezo-catalysis but can be accomplished by CEC. Besides, the outstanding H_2O_2 generation rate of CEC via indirect $2e^-$ WOR was significantly higher than that of piezo-catalysis via $2e^-$ ORR in Fig. 2b, implying the superior advantage of WOR over ORR for H_2O_2 evolution due to the IEF induced by CE effect.

The detailed H_2O_2 evolution process in FCPs/CEC as depicted in Fig. 2f. The overlap of electron clouds between the F atom (FCPs) and the O atom (H_2O) upon contact under ultrasonic excitation lowered the potential barrier[42], resulting in the transfer of electrons from H_2O to FCP, driven by the exceptional electron-withdrawing capacity of F and reduced electron transfer barriers under ultrasound[28]. After being separated, the transferred electrons remained as static charges and accumulated on the FCP surface, ultimately yielding $H_2O^{•+}$and FCP* (Eqs. 6–7). Immediately, the $H_2O^{•+}$ reacted with neighboring H_2O and ultimately combining to form H_3O^+ and $^*OH$ (Eq. 8). Simultaneously, the accumulated electrons on FCPs surface induced an IEF, thereby facilitating the indirect $2e^-$ WOR processes by lowering the activation energy barrier and subsequently promoting the recombination of $^*OH$ into H_2O_2 (Eq. 5). The sustained reducing activity of FCP, due to the accumulated surface electrons, facilitated the conversion of O_2 to $O_2^{•-}$, further contributing to H_2O_2 evolution pathways (Eqs. 9–12)[43]. Reports indicated that the free radicals tended to react with each other rather than disperse in the solution due to the Grotthuss mechanism through the hydrogen bond network of water in FCP/CEC[23]. Furthermore, considering the excellent electron gain/loss ability of unpaired electrons in $^*OH$, the F within FCP, renowned for their superb electron-withdrawing capacity, were anticipated to interact with $^*OH$, concentrating $^*OH$ around the FCP interface, and promoting their chances of recombination into H_2O_2[44]. In conclusion, the enhanced formation and recombination of $^*OH$ ultimately led to the heightened generation of H_2O_2 in FCP/CEC, showcasing the significant role of IEF induced by the CE effect in this intricate catalytic process.

$$H_2O \rightarrow H_2O^{•+} + e^- \tag{6}$$

$$FCP + e^- \rightarrow FCP^* \tag{7}$$

$$H_2O^{•+} + H_2O \rightarrow H_3O^+ + {}^*OH \tag{8}$$

$$O_2 + e^- \rightarrow O_2^{•-} \tag{9}$$

$$O_2^{•-} + H^+ \rightarrow HO_2^{•} \tag{10}$$

$$O_2^{•-} + HO_2^{•} \rightarrow HO_2^{-} + O_2 \tag{11}$$

$$HO_2^{-} + H^+ \rightarrow H_2O_2 \tag{12}$$

The FEP/CEC demonstrated a consistent ability to generate H_2O_2 across a broad pH range from 2.6 to 9.6 (Supplementary Fig. 5). This wide operational pH range highlighted its versatility and potential to adapt to diverse pH conditions commonly found in wastewater treatment scenarios. Furthermore, the steady accumulation of H_2O_2 within FEP/CEC over a 4 h period indicated the stability of the chemically inert FEP during the H_2O_2 evolution process (Supplementary Fig. 6). The impact of various anions such as Cl^-, SO_4^{2-}, and HPO_4^{2-} on H_2O_2 yield was minimal, suggesting their limited interference with H_2O_2 production in FEP/CEC (Supplementary Fig. 7). However, the addition of CO_3^{2-} notably inhibited H_2O_2 production in FEP/CEC, leading to a 62.33% decrease. This inhibitory effect could be attributed to the ions shielding effect, resulting in compromised electron transfer, or the interaction between CO_3^{2-} and $^*OH$[10]. Notably, these two inhibitory effects were not observed in the presence of other anions. The distinct influence of CO_3^{2-} on H_2O_2 production in FEP/CEC warrants further exploration in future research to elucidate the underlying mechanisms responsible for this phenomenon. Based on the aforementioned results, the FEP/CEC exhibited the advantages of remarkable and stable H_2O_2 accumulation, meeting the prerequisites for achieving the SC-Fenton system.

Water purification by Fe^{III}/FEP/CEC SC-Fenton system

In the pursuit of water purification efficacy utilizing the Fe^{III}/FEP/CEC SC-Fenton system, a detailed investigation into its catalytic degradation process was undertaken using SDZ as the model pollutant. Supplementary Fig. 8 illustrates that ultrasound alone (US) and Fe^{III}/US both exhibited minimal impact on SDZ degradation. Notably, FEP/CEC accomplished 68.59% of SDZ removal with an accumulation of 0.62 mM H_2O_2 (Supplementary Fig. 9). This outcome aligned with the observation that $^*OH$ tended to react with each other, generating H_2O_2 instead of directly attacking SDZ. This behavior was not only ascribed to the interaction between $^*OH$ and FCP, but also due to the higher reactivity of 2 $^*OH$ ($k_{(*OH/*OH)} = 5.2 \times 10^9\ M^{-1} \cdot s^{-1}$) with each other compared to SDZ ($k_{(*OH/SDZ)} = 1.9 \times 10^9\ M^{-1} \cdot s^{-1}$)[10], leading to H_2O_2 accumulation through $^*OH$ recombination, even in the presence of SDZ. This suggested that $^*OH$ via CEC primarily engaged in the recombined reaction, forming H_2O_2 rather than catalytic degradation. Exploring the utilization of generated H_2O_2 was deemed crucial to enhance the catalytic degradation capability of CEC. The ineffectiveness of SDZ degradation in H_2O_2/US ruled out the potential of ultrasound in activating H_2O_2 for pollutant removal (Supplementary Fig. 10). Given that the Fenton reaction, known for decomposing H_2O_2 via iron regent, is widely employed, Fe^{III} homogeneous reagent ($FeCl_3$ of 1.0 mM) was introduced to initiate the SC-Fenton (Fe^{III}/FEP/CEC). The concentration of H_2O_2 was very low in Fe^{III}/FCP/CEC, demonstrating that the generated H_2O_2 via FCP/CEC process was consumed in the presence of Fe^{III}, further suggesting the existence of SC-Fenton process in the Fe^{III}/FCP/CEC (Supplementary Fig. 9). Figure 3a showcased that the SDZ removal rate of Fe^{III}/FEP/CEC (0.125 min^{-1}) was 5.43-fold of that in FEP/CEC (0.023 min^{-1}), highlighting the enhanced catalytic degradation effect of SC-Fenton. Furthermore, the Fe^{III} as the iron source demonstrated superior degradation performance (2.30-fold) compared to Fe^{II}, in line with previous reported self-cycled Fenton systems[15,45]. Moreover, the total organic carbon (TOC) removal profiles observed in all three systems exhibited strong correlations with their SDZ degradation efficiencies (Supplementary Fig. 11), confirming that the Fe^{III}/FEP/CEC achieved not only unparalleled degradation kinetics but also superior mineralization efficiency. Additional SC-Fenton systems were constructed with PTFE and PVDF as CEC catalysts, leading to significant enhancements in degradation efficiency (2.68–4.28 times) and reaction rates compared to their respective control groups (Fig. 3b). These findings suggested that Fe^{III}/FCP/CEC SC-Fenton can be tailored by incorporating various FCPs as CEC catalysts. Moreover, the efficient removal of other pollutants (PE, CBZ, and ATR) with diverse molecular structures were also achieved by Fe^{III}/FEP/CEC (Fig. 3c). Furthermore, Fe^{III}/FEP/CEC exhibited better degradation performance than that of previous piezo- and photo-catalysis induced SC-Fenton systems (Supplementary Table 4). Consequently, Fe^{III}/FCP/CEC exhibited remarkable catalytic oxidation capacity for water purification.

The pH value was a pivotal factor influencing traditional Fenton and Fenton-like catalytic degradation performance[46,47]. As shown in Fig. 4a, there were minimal differences in SDZ degradation rate in Fe^{III}/FEP/CEC across a range of initial pH values (3.6 to 9.6), indicating its robust degradation capacity without requiring pH adjustment. In fact, the introduction of $FeCl_3$ triggered a pronounced pH decrease (Supplementary Fig. 12), a phenomenon governed by Fe^{3+} hydrolysis that simultaneously imparts

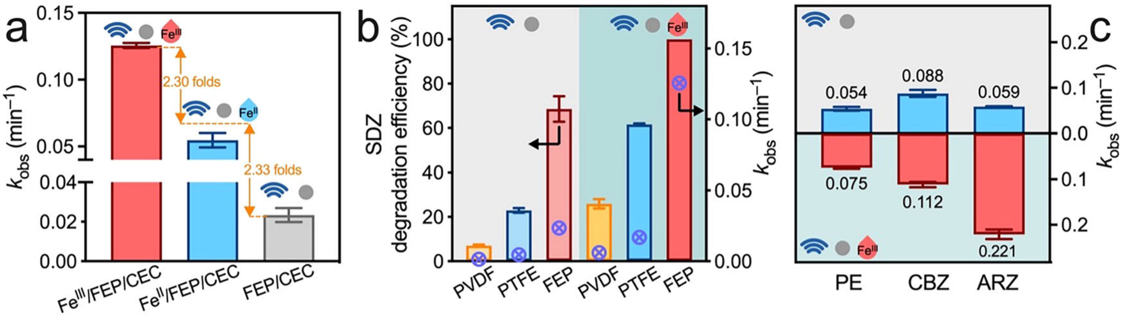

Fig. 3 | Water purification performance of Fe^{III}/FCP/CEC. The pseudo-first order k_{obs} of SDZ degradation by Fe^{III}/FEP/CEC, Fe^{II}/FEP/CEC, and FEP/CEC (**a**). The SDZ degradation efficiency and pseudo-first order k_{obs} of FCP/CEC and Fe^{III}/FCP/CEC (**b**). The comparison of pseudo-first-order k_{obs} of different pollutants by Fe^{III}/FEP/CEC (**c**). Experimental conditions: $[FCPs]_0 = 0.1\ g{\cdot}L^{-1}$, $[Fe^{III}] = 1\ mM$, $[Pollutant] = 5\ mg{\cdot}L^{-1}$, T = 25 ± 2 °C.

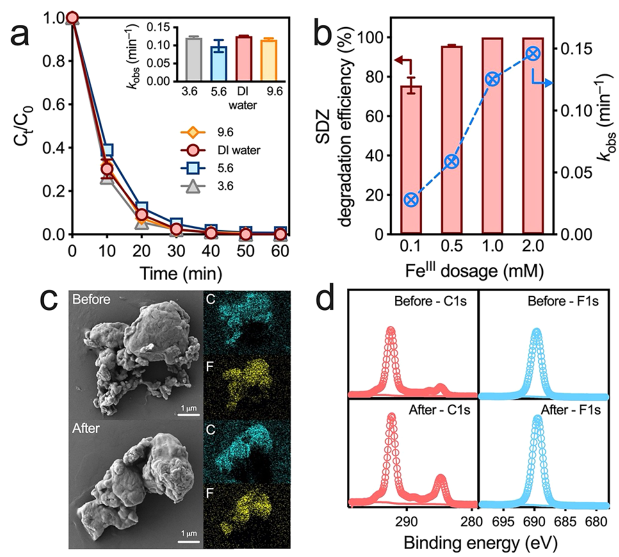

Fig. 4 | Potential application for water purification by the Fe^{III}/FEP/CEC. The effect of initial pH condition on SDZ removal in Fe^{III}/FEP/US (**a**). The SDZ removal in Fe^{III}/FEP/US with different dosages of Fe^{s} (**b**). The SEM (**c**) and XPS (**d**) of FEP before and after reaction. Experimental conditions: $[FCPs]_0 = 0.1\ g{\cdot}L^{-1}$, $[SDZ] = 5\ mg{\cdot}L^{-1}$, T = 25 ± 2 °C.

Lewis acidity and enhances solution's acidity[48–50]. This autogenous acidification serves dual functions: it prevents iron precipitation through pH modulation while inherently addressing the solubility challenges of conventional Fenton processes. Remarkably, the Fe^{III}/FEP/CEC system maintains stable iron dispersion even in alkaline wastewater matrices (initial pH >7.0), demonstrating exceptional operational pH flexibility. By leveraging $FeCl_3$'s intrinsic hydrolytic properties, the system circumvents the need for external acid supplementation-a critical limitation in traditional Fenton processes-thereby achieving self-regulated iron solubility across diverse pH conditions. The SDZ degradation rate increased along with the dosage of Fe^{III}, elevating from 0.1 to 2.0 mM (Fig. 4b). Additionally, the Fe^{III}/FEP/CEC demonstrated its catalytic stability after five cycles (Supplementary Fig. 13). Structural and compositional analysis of FCPs through pre- and post-reaction characterization confirmed the absence of detectable morphological alterations or chemical modifications following multiple reuse cycles under ultrasonication (Fig. 4c, d and Supplementary Figs. 14–16). This exceptional stability highlights the inherent durability of FCPs, consistent with their documented chemical inertness and resistance to structural degradation under operational conditions[43]. The preservation of both physical architecture and molecular integrity across reaction cycles substantiates FCPs' reliability as robust catalysts in sustained catalytic applications. Despite the slight inhibition of common anions on degradation performance due to their impact on H_2O_2 yield and the scavenging role on ROS (Supplementary Fig. 17), the Fe^{III}/FEP/CEC maintained commendable performance in water purification endeavors.

Table 1 | The comparison of *OH in FEP/CEC and $^{\bullet}$OH in Fe^{III}/FEP/CEC

	*OH	$^{\bullet}$OH
Meaning	Interfacial hydroxyl radical	Dissociative hydroxyl radical
Precursor	H_2O	H_2O_2
Generated pathways	$H_2O \rightarrow H_2O^{\bullet+} + e^-$ $H_2O^{\bullet+} + H_2O \rightarrow H_3O^+ + {}^{*}OH$	$Fe^{II} + H_2O_2 \rightarrow Fe^{III} + {}^{\bullet}OH + OH^-$
Generated system	FEP/CEC	Fe^{III}/FEP/CEC SC-Fenton
Distribution	Mainly at the interface of FEP	Liquid solution
Dominant role	Recombination into H_2O_2 ${}^{*}OH + {}^{*}OH \rightarrow H_2O_2$	Degradation pollutant

Mechanism of Fe^{III}/FEP/CEC SC-Fenton system

In the FEP/CEC system, interfacial *OH recombine to form H_2O_2, while in the Fe^{III}/FEP/CEC-based SC-Fenton configurations, H_2O_2 undergoes catalytic decomposition to generate dissociative $^{\bullet}$OH, responsible for contaminant breakdown. To systematically evaluate catalytic performance, we specifically analysed $^{\bullet}$OH production through the Fe^{III}-mediated Fenton reaction as the primary descriptor of pollutant degradation efficiency. This distinction between *OH (H_2O_2 precursor) and Fenton-generated $^{\bullet}$OH (pollutant degradation) was displayed in Table 1 to clarify their respective roles. Isopropanol (IPA) known as a scavenger for $^{\bullet}$OH ($k_{(\bullet OH/IPA)} = 1.6 \times 10^{10}\ M^{-1}{\cdot}s^{-1}$)[51], was introduced into FEP/CEC and Fe^{III}/FEP/CEC to assess the role of $^{\bullet}$OH in SDZ degradation. As depicted in Fig. 5a and Supplementary Fig. 18, the addition of IPA (100 mM) effectively halted the oxidation of SDZ in both FEP/CEC and Fe^{III}/FEP/CEC, indicating the crucial involvement of $^{\bullet}$OH in these systems. Additionally, $O_2^{\bullet-}$ also contributed to catalytic degradation, as evidenced by a decrease in removal efficiency of 23.2 and 65.1% in FEP/CEC and Fe^{III}/FEP/CEC, respectively, in the presence of *p*-BQ ($k_{(O_2\bullet-/p\text{-}BQ)} = 0.9 \times 10^9\ M^{-1}{\cdot}s^{-1}$)[52]. The marginal inhibition by β-carotene suggested the participation of $^1O_2$ in SDZ remediation. To verify potential high-valent iron species formation, we employed methyl phenyl sulfoxide (PMSO) as a probe ($k_{(FeIV/PMSO)} = 1.23 \times 10^5\ M^{-1}{\cdot}s^{-1}$) in Fe^{III}/FCP/CEC systems[53]. The complete absence of methyl phenyl sulfone ($PMSO_2$) generation during SDZ degradation conclusively demonstrates the non-participation of Fe^{IV} intermediates in these catalytic processes (Fig. 5b and Supplementary Fig. 19). These selective ROS screening tests underscored the pivotal role of •OH in SDZ degradation, followed by $O_2^{\bullet-}$ and $^1O_2$, in both FeIII/FEP/

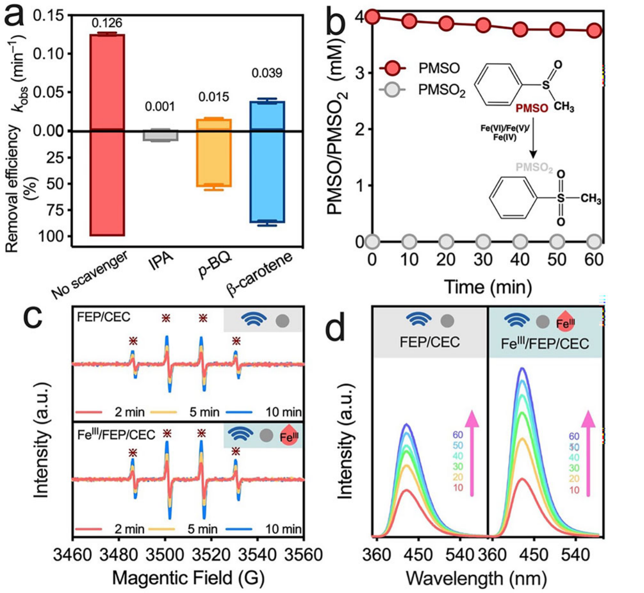

Fig. 5 | Investigation into reactive oxygen species in Fe^{III}/FEP/CEC. The inhibited effect from different scavengers on SDZ degradation performance in Fe^{III}/FEP/CEC (**a**). The PMSO consumption and $PMSO_2$ formation in Fe^{III}/FEP/CEC over time (**b**). The EPR signals of DMPO-$^{\bullet}$OH of FEP/CEC and Fe^{III}/FEP/CEC (**c**). The self-quantitative analysis of $^{\bullet}$OH yield in FEP/CEC and Fe^{III}/FEP/CEC (**d**). Experimental conditions: $[FCPs]_0 = 0.1$ g·L^{-1}, $[Fe^{III}] = 1$ mM, T = 25 ± 2 °C.

CEC and FEP/CEC. This evidence aligns with the system's exclusive $^{\bullet}$OH-mediated degradation mechanism, reaffirming the dominance of SC-Fenton chemistry over alternative high-valent iron pathways under the investigated conditions. To elucidate the enhanced degradation performance of FCPs/CEC and Fe^{III}/FCPs/CEC, the yield of $^{\bullet}$OH, a critical descriptor, was further investigated. Firstly, the relative intensity of DMPO-$^{\bullet}$OH in Fe^{III}/FEP/CEC surpassed that of FEP/CEC, indicating that Fe^{III} expedited $^{\bullet}$OH production (Fig. 5c). Secondly, the catalytic enhancement of Fe^{III} on $^{\bullet}$OH yield was further analyzed. As shown in Fig. 5d, both FEP/CEC and Fe^{III}/FEP/CEC exhibited time-dependent intensification of fluorescent peaks corresponding to $^{\bullet}$OH accumulation. Notably, the Fe^{III}-modified system showed enhanced fluorescent signals compared to its Fe^{III}-free counterpart at equivalent reaction intervals. Consistent with these observations, parallel experiments in PTFE- and PVDF-based systems revealed analogous Fe^{III}-mediated amplification of $^{\bullet}$OH yield (Supplementary Fig. 19), demonstrating the universal catalytic capacity of Fe^{III} to amplify $^{\bullet}$OH generation across all FCP/CEC configurations in the SC-Fenton system. These systematic comparisons establish dual functionality of Fe^{III} as both an electron transfer mediator and radical production accelerator through facilitated interfacial redox cycling.

The higher $^{\bullet}$OH generation in Fe^{III}/FEP/CEC was potentially attributed to the generated Fe^{II} triggering the Fenton process by activating H_2O_2. Consequently, the reduction regime of Fe^{III} into Fe^{II} in FEP/CEC was further elucidated. The concentrations of Fe species (Fe^{III} and Fe^{II}) in FEP/CEC were shown in Fig. 6a, b according to the 1,10-phenanthroline spectrophotometry based on the absorbance of orange-red product between Fe^{II} and 1,10-phenanthroline (details in Supplementary Note 1.1). Quantitative analysis revealed that the content of Fe^{III} remained constant at close to 100% without detectable Fe^{II} accumulation during the reaction. This absence of Fe^{II} species originates from immediate Fenton consumption of nascent Fe^{II} by continuously generated H_2O_2. Consequently, in ex situ chemical analysis using 1,10-phenanthroline, Fe^{II} remained undetectable due to its instantaneous reaction with H_2O_2 prior to sampling. To resolve this detection limitation, an in situ chemical analysis was implemented by introducing 1,10-phenanthroline directly into the Fe^{III}/FCP/CEC system, enabling real-time sequestration of

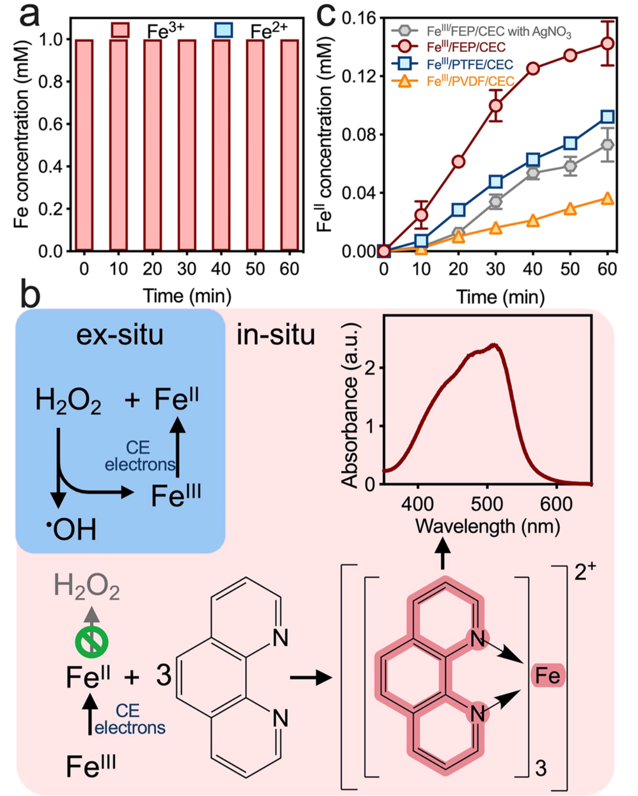

Fig. 6 | Fe^{III}/Fe^{II}cycle in Fe^{III}/FEP/CEC. The concentration changes of Fe^{II} and Fe^{III} overtime in Fe^{III}/FEP/CEC by ex situ 1,10-phenanthroline method (**a**). The schematic of detection procedures for Fe^{II} and Fe^{III} overtime in Fe^{III}/FEP/CEC by ex situ and in situ 1,10-phenanthroline methods (**b**). The real-time Fe^{II} concentration dynamics in Fe^{III}/FEP/CEC by in situ 1,10-phenanthroline method (**c**). Experimental conditions: $[FCPs]_0 = 0.1$ g·L^{-1}, $[Fe^{III}] = 1$ mM, T = 25 ± 2 °C.

transient Fe^{II} species (details in Supplementary Note 1.2 and Supplementary Fig. 20)[15]. As shown in Fig. 6c, the gradually increasing concentration of Fe^{II} in Fe^{III}/FCP/CEC indicated the existence of fresh Fe^{II} as the reducing intermediate of Fe^{III}, suggesting a rapid cycling process between Fe^{III} and Fe^{II}. The reduction of Fe^{III} into Fe^{II} was likely facilitated by the reductive CE electrons. Previous studies have indicated that CE electrons were able to reduce various high-valent metal ions to low-valent states in an aqueous solution, with reduction potentials ranging from 0.643 to 1.156 V vs. SHE[25]. The reduction potential of the Fe^{III}/Fe^{II} process ($Fe^{III} + e^- \rightarrow Fe^{II}$) was 0.77 V vs. SHE, which was supposed to be achieved in FEP/CEC. Furthermore, the in situ quantitative results revealed that the accumulation of fresh Fe^{II} followed the order of FEP > PTFE > PVDF (Fig. 6c), aligning with the available contact charge amount of the three FCPs. The addition of $AgNO_3$ as the electron scavenger further inhibited the accumulation of fresh Fe^{II}, demonstrating the role of CE electrons in the reduction and transformation from Fe^{III} to Fe^{II}. The electron transfer process between FEP and Fe^{III} was corroborated by the electrochemical method. As shown in Supplementary Fig. 21, the addition of Fe^{III} increased the potential, indicating electron transfer from FEP to Fe^{III} [15,54]. Additionally, the built IEF via accumulated electrons on the FCP surface attracted the Fe^{III} ions due to the electrostatic induction, facilitating the electron transfer from the FCP surface to Fe^{III}. Thus, the Fe^{II} was generated via the Fe^{III} reduction by CE (Eq. 13).

While Fe^{III} generated through the Fenton reaction in the Fe^{II}/FEP/CEC (Eq. 14) was reduced to Fe^{II} via CE electrons[55], a critical operational distinction arises: the Fe^{II}/FEP/CEC system starts with preloaded Fe^{II}, whereas H_2O_2 accumulates progressively during the reaction. This stoichiometric mismatch creates an excess of Fe^{II} relative to H_2O_2 availability, triggering parasitic $^{\bullet}$OH quenching through Fe^{II}–$^{\bullet}$OH interactions (Eq. 15)[56], which

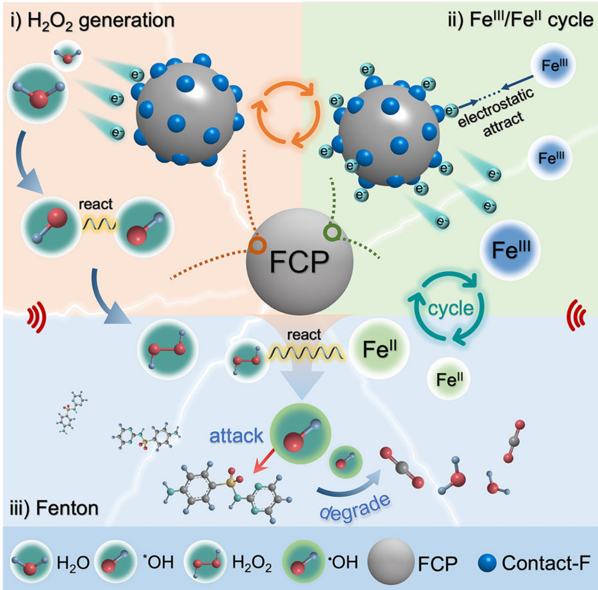

Fig. 7 | The schematic of FCP/CEC-driven self-cycled Fenton: a mechanistic framework for energy-autonomous water purification.

diminishes oxidative efficiency. Conversely, the Fe^{III}/FEP/CEC maintains controlled Fe^{II} regeneration without iron overaccumulation, thereby suppressing radical scavenging pathways. This mechanistic divergence underpins the enhanced degradation performance of Fe^{III}/FEP/CEC over its Fe^{II} counterpart. Furthermore, dose-independent kinetic studies further demonstrated non-proportional behavior, where increasing $FeCl_3$ concentrations from 1 mM ($k_{obs} = 0.125\ min^{-1}$) to 2 mM ($k_{obs} = 0.146\ min^{-1}$) resulted in only 16.8% rate enhancement. The sublinear increase implies competitive •OH consumption by surplus Fe^{II} at elevated catalyst loads, highlighting the necessity for optimizing $FeCl_3$ dosage to maximize system efficacy. Although the reaction between H_2O_2 and Fe^{III} could generate •OOH and lead to the formation of $^1O_2$ for pollutants degradation[1,45], this sluggish reaction was deemed too slow to be considered the primary reduction pathway (Eq. 16). Besides, the H_2O_2 decomposition process exhibited direct proportionality to fresh Fe^{II} generation rates, as evidenced by the system-dependent hierarchy: Fe^{III}/FEP/CEC displayed maximal H_2O_2 consumption (the reduction of H_2O_2 yield between FEP/CEC and Fe^{III}/FEP/CEC, $\Delta[H_2O_2] = 0.55$ mM) concurrent with peak Fe^{II} accumulation (0.14 mM), followed by Fe^{III}/PTFE/CEC ($\Delta[H_2O_2] = 0.28$ mM; $Fe^{II} = 0.09$ mM) and Fe^{III}/PVDF/CEC ($\Delta[H_2O_2] = 0.05$ mM; $Fe^{II} = 0.03$ mM). These quantitative correlations confirm the operational SC-Fenton mechanism wherein H_2O_2 undergoes continuous decomposition through Fe^{II}-catalyzed reactions, sustaining redox cycling between Fe^{III}/Fe^{II} states. (Supplementary Fig. 9). Consequently, the cycling process between Fe^{III} and Fe^{II} was divided into two steps: (i) the Fe^{III} acquired one CE electron and reduced into Fe^{II}, and (ii) the Fe^{II} promptly activated the generated H_2O_2 and transformed back into Fe^{III}.

$$Fe^{III} + CE \rightarrow Fe^{II} \tag{13}$$

$$Fe^{II} + H_2O_2 \rightarrow Fe^{III} + {}^{\bullet}OH + OH^- \; k = 53 - 76\, M^{-1} \cdot s^{-1} \tag{14}$$

$$Fe^{II} + {}^{\bullet}OH \rightarrow Fe^{III} + OH^- \; k = 3.2 - 4.3 \times 10^8\, M^{-1} \cdot s^{-1} \tag{15}$$

$$Fe^{III} + H_2O_2 \rightarrow Fe^{II} + HO_2^{\bullet} + H^+ \; k = 0.001 - 0.01\, M^{-1} \cdot s^{-1} \tag{16}$$

Figure 7 illustrates the Fe^{III}/FEP/CEC mechanism for pollutant degradation through three sections: (i) H_2O_2 generation via ultrasound-triggered contact-electrification (CE), where electron transfer from H_2O to the FEP surface, yielding $^*OH$ and electron-rich FEP*. Subsequently, the induced interfacial electric field (IEF) on FEP* promoted the H_2O_2 generation via lowering the free energy for the $^*OH$ recombination into H_2O_2 via the indirect $2e^-$ process. (ii) Fe^{III} reduction into Fe^{II}, where accumulated CE electrons on the FEP* surface reduced Fe^{III} while FEP* returned to its original uncharged state as FEP to initiate a new cycle of H_2O_2 generation. (iii) Fenton-driven water purification, where the generated H_2O_2 and Fe^{II} initiate the Fenton reaction, producing •OH to degrade pollutants. Concurrently, the Fe^{III} generated from the Fenton reaction went through a new reduction into Fe^{II} by CE electrons on FEP* as shown in section ii). This Fe^{III}/FEP/CEC triggered self-cycled Fenton by simultaneous H_2O_2 production and Fe^{III} reduction into Fe^{II} in one system, ultimately achieving efficient water purification.

Discussion

This study presents a novel Fe^{III}/FEP/CEC system that resolves critical limitations in self-cycled Fenton reactions by synergistically integrating H_2O_2 generation and Fe^{III} reduction within a unified catalytic platform. The FEP/CEC configuration demonstrates particular significance, achieving superior H_2O_2 accumulation (7.67 $mmol \cdot g_{cat}^{-1} \cdot h^{-1}$) through an indirect $2e^-$ WOR. This performance enhancement originates from the established IEF, which effectively lowers the free energy for $^*OH$ formation and subsequent recombination into H_2O_2. Simultaneously, the system facilitates the continuous regeneration of Fe^{II} through triboelectrically driven Fe^{III} reduction, amplifying •OH yields compared to conventional Fenton systems and thereby elevating overall pollutant degradation efficiency. Our findings validate the technical viability of self-cycled Fenton processes through the strategic coupling of Fe^{III} and FEP/CEC, propelling the engineering of energy-autonomous water purification systems. Beyond immediate applications, this work stimulates synergistic exploitation of FEP/CEC's dual oxidative-reductive functionalities, as evidenced by its capacity to simultaneously drive H_2O_2 synthesis (oxidative pathway) and Fe^{III} activation (reductive pathway). Such bifunctional capability not only advances water treatment technologies but also establishes a paradigm for designing multifunctional catalytic systems to address environmental remediation challenges.

Methods

Chemicals and materials

All the chemical reagents were provided in Supplementary Note 2 and Supplementary Table 1.

Experimental procedures

The performance of H_2O_2 generation by FCPs/CEC (FCPs: fluorinated ethylene propylene (FEP, average 5 μm), polytetrafluoroethylene (PTFE, <d> ~1–5 μm), and polyvinylidene fluoride (PVDF, average 6.5 μm) were investigated in an ultrasound bath (BRANSON, 3800-CPXH, USA) at 25 ± 2 °C, along with 40 kHz and 110 W. The 3 mg of different FCPs ($0.1\ g \cdot L^{-1}$) were dispersed into 30 mL deionized water. At the time intervals, 3 mL of liquid sample was withdrawn and filtered with 0.22 μm polyethersulfone membranes for subsequent H_2O_2 concentration analysis. The pH was not adjusted except as specifically mentioned with 1.0 M of HCl or NaOH.

The catalytic degradation performance of FCPs/CEC SC-Fenton system were investigated with $FeCl_3$ (1.0 mM except as specifically mentioned) as iron precursor added into the ultrasound bath. The 5 $mg \cdot L^{-1}$ of sulfadiazine (SDZ), carbamazepine (CBZ), phenol (PE), and atrazine (ATR) were selected as target pollutants to test degradation ability without pH adjustment except as mentioned. All the degradation reaction was conducted under ultrasound irradiation (40 kHz, 110 W) at 25 ± 2 °C. At a certain time interval, 1 mL of liquid sample was withdrawn and filtered by 0.22 μm polyethersulfone membranes and quenched by methanol for further analysis of the target pollutants concentration. The FCPs after reactions were separated from liquid by a vacuum filtration system and washed with ethanol, followed by drying 50 °C overnight before reutilization or analysis.

Analytical methods

The concentration of H_2O_2 was determined by the potassium titanium (IV) oxalate method[57]. Detailly, the potassium titanium (IV) oxalate solution was prepared via 7.083 g of potassium titanium (IV) oxalate adding into 10 M of H_2SO_4. Here, 2 mL of filtered sample, 2 mL of potassium titanium (IV) oxalate solution, and 1 mL deionized water were mixed for 5 min, and the absorbance of the mixture was further measured by a spectrophotometer (Thermo, Evolution 220, USA) at 400 nm. The H_2O_2 concentration was quantitatively calculated by the standard curve ($R^2 = 0.9998$) in Supplementary Fig. 1. The relative quantitative analysis of hydroxyl radical was conducted by a fluorescence method in Supplementary Note 3. The detection of reactive species was utilized by EPR spectroscopy (Supplementary Note 4). The concentrations of pollutants were analyzed using UPLC (Waters, H-CLASS, USA) equipped with PDA detector and C18 column with flowing rate of 0.2 $mL \cdot min^{-1}$. More parameters of the mobile phase and detection wavelength were provided in Supplementary Table 5. The concentration of Fe species was carried out in accordance with the details in Supplementary Note 1. The density functional theory (DFT) calculation was conducted according to the details in Supplementary Note 5. The transferred electrons of the FCP surface were analyzed by the single electrode triboelectric nanogenerator (SETENG) based on the Supplementary Note 6.

Data availability

No datasets were generated or analysed during the current study.

Received: 3 March 2025; Accepted: 9 May 2025;
Published online: 20 May 2025

References

1. Zhou, P. et al. Fast and long-lasting iron(III) reduction by boron toward green and accelerated Fenton chemistry. *Angew. Chem. Int. Ed.* **59**, 16517–16526 (2020).
2. Shi, Y. et al. Defect-engineering-mediated long-lived charge-transfer excited-state in Fe–gallate complex improves iron cycle and enables sustainable Fenton-like reaction. *Adv. Mater.* **36**, 2305162 (2024).
3. Mao, Y. et al. Accelerating Fe^{III}-aqua complex reduction in an efficient solid–liquid-interfacial Fenton reaction over the Mn–CNH co-catalyst at near-neutral pH. *Environ. Sci. Technol.* **55**, 13326–13334 (2021).
4. Liu, J. et al. Molybdenum sulfide co-catalytic Fenton reaction for rapid and efficient inactivation of *Escherichia coli*. *Water Res.* **145**, 312–320 (2018).
5. Wu, Y., Che, H., Liu, B. & Ao, Y. Promising materials for photocatalysis-self-Fenton system: properties, modifications, and applications. *Small Struct.* **4**, 2200371 (2023).
6. Wu, Y. et al. Boosting 2e$^-$ oxygen reduction reaction in garland carbon nitride with carbon defects for high-efficient photocatalysis-self-Fenton degradation of 2,4-dichlorophenol. *Appl. Catal. B* **307**, 121185 (2022).
7. Wang, F. et al. Unprecedentedly efficient mineralization performance of photocatalysis-self-Fenton system towards organic pollutants over oxygen-doped porous g-C_3N_4 nanosheets. *Appl. Catal. B* **312**, 121438 (2022).
8. Zhang, X. et al. Resin-based photo-self-Fenton system with intensive mineralization by the synergistic effect of holes and hydroxyl radicals. *Appl. Catal. B* **315**, 121525 (2022).
9. Fu, C. et al. Dual-defect enhanced piezocatalytic performance of C_3N_5 for multifunctional applications. *Appl. Catal. B* **323**, 122196 (2023).
10. Wang, Y. et al. O_2-independent H_2O_2 production via water–polymer contact electrification. *Environ. Sci. Technol.* **58**, 925–934 (2024).
11. Shi, X. et al. Understanding activity trends in electrochemical water oxidation to form hydrogen peroxide. *Nat. Commun.* **8**, 701 (2017).
12. Siahrostami, S. et al. A review on challenges and successes in atomic-scale design of catalysts for electrochemical synthesis of hydrogen peroxide. *ACS Catal.* **10**, 7495–7511 (2020).
13. Nosaka, Y. & Nosaka, A. Y. Generation and detection of reactive oxygen species in photocatalysis. *Chem. Rev.* **117**, 11302–11336 (2017).
14. Perry, S. C. et al. Electrochemical synthesis of hydrogen peroxide from water and oxygen. *Nat. Rev. Chem.* **3**, 442–458 (2019).
15. Xu, J. et al. Highly efficient Fe^{III}-initiated self-cycled Fenton system in piezo-catalytic process for organic pollutants degradation. *Angew. Chem. Int. Ed.* **62**, e202307018 (2023).
16. Hu, X. et al. Engineering nonprecious metal oxides electrocatalysts for two-electron water oxidation to H_2O_2. *Adv. Energy Mater.* **12**, 2201466 (2022).
17. Siahrostami, S., Li, G.-L., Viswanathan, V. & Nørskov, J. K. One- or two-electron water oxidation, hydroxyl radical, or H_2O_2 evolution. *J. Phys. Chem. Lett.* **8**, 1157–1160 (2017).
18. Ma, J. et al. H_2O_2 photosynthesis from H_2O and O_2 under weak light by carbon nitrides with the piezoelectric effect. *J. Am. Chem. Soc.* **146**, 21147–21159 (2024).
19. Li, S. et al. Contributions of different functional groups to contact electrification of polymers. *Adv. Mater.* **32**, 2001307 (2020).
20. Wang, Z., Dong, X., Tang, W. & Wang, Z. L. Contact-electro-catalysis (CEC). *Chem. Soc. Rev.* **53**, 4349–4373 (2024).
21. Chen, B. et al. Water–solid contact electrification causes hydrogen peroxide production from hydroxyl radical recombination in sprayed microdroplets. *Proc. Natl Acad. Sci. USA* **119**, e2209056119 (2022).
22. Zou, H. et al. Quantifying the triboelectric series. *Nat. Commun.* **10**, 1427 (2019).
23. Berbille, A. et al. Mechanism for generating H_2O_2 at water-solid interface by contact-electrification. *Adv. Mater.* **35**, 2304387 (2023).
24. Zhao, J. et al. Contact-electro-catalysis for direct synthesis of H_2O_2 under ambient conditions. *Angew. Chem. Int. Ed.* **62**, e202300604 (2023).
25. Su, Y. S. et al. Reduction of precious metal ions in aqueous solutions by contact-electro-catalysis. *Nat. Commun.* **15**, 4196 (2024).
26. Nie, J. et al. Probing contact-electrification-induced electron and ion transfers at a liquid–solid interface. *Adv. Mater.* **32**, 1905696 (2020).
27. Yuan, X., Zhang, D., Liang, C. & Zhang, X. Spontaneous reduction of transition metal ions by one electron in water microdroplets and the atmospheric implications. *J. Am. Chem. Soc.* **145**, 2800–2805 (2023).
28. Ma, D. et al. Fluorocarbon polymers mediated contact-electro-catalysis activating peroxymonosulfate for emerging pollutants degradation: the key role of fluorine density in electron transfer. *Chem. Eng. J.* **497**, 154996 (2024).
29. Wu, Y. et al. Triggering dual two-electron pathway for H_2O_2 generation by multiple [Bi−O]n interlayers in ultrathin $Bi_{12}O_{17}Cl_2$ towards efficient piezo-self-Fenton catalysis. *Angew. Chem. Int. Ed.* **63**, e202316410 (2024).
30. Wei, Y., Zhang, Y., Geng, W., Su, H. & Long, M. Efficient bifunctional piezocatalysis of Au/$BiVO_4$ for simultaneous removal of 4-chlorophenol and Cr(VI) in water. *Appl. Catal. B* **259**, 118084 (2019).
31. Feng, J. et al. Significant improvement and mechanism of ultrasonic inactivation to *Escherichia coli* with piezoelectric effect of hydrothermally synthesized t-$BaTiO_3$. *ACS Sustain. Chem. Eng.* **6**, 6032–6041 (2018).
32. Shao, D., Zhang, L., Sun, S. & Wang, W. Oxygen reduction reaction for generating H_2O_2 through a piezo-catalytic process over bismuth oxychloride. *ChemSusChem* **11**, 527–531 (2018).
33. Wang, K. et al. Ternary BaCaZrTi perovskite oxide piezocatalysts dancing for efficient hydrogen peroxide generation. *Nano Energy* **98**, 107251 (2022).
34. Zeng, H. et al. Boost piezocatalytic H_2O_2 production in $BiFeO_3$ by defect engineering enabled dual-channel reaction. *Mater. Today Energy* **39**, 101475 (2024).
35. Cui, Y. et al. Harvesting vibration energy to produce hydrogen peroxide with Bi_3TiNbO_9 nanosheets through a water oxidation dominated dual-channel pathway. *ACS Sustain. Chem. Eng.* **12**, 3595–3607 (2024).

36. Deng, M., Wang, D. & Li, Y. General design concept of high-performance single-atom-site catalysts for H_2O_2 electrosynthesis. *Adv. Mater.* **36**, 2314340 (2024).
37. Li, W. et al. Contact-electro-catalysis for direct oxidation of methane under ambient conditions. *Angew. Chem. Int. Ed.* **63**, e202403114 (2024).
38. Dong, X. et al. Regulating contact-electro-catalysis using polymer/metal janus composite catalysts. *J. Am. Chem. Soc*. https://doi.org/10.1021/jacs.4c07446 (2024).
39. Liu, N., Wang, R., Zhao, J., Jiang, J. & Fan, F. R. Piezoelectricity and triboelectricity enhanced catalysis. *NRE*. https://doi.org/10.26599/NRE.2024.9120137 (2024).
40. Liu, J. et al. Nonaqueous contact-electro-chemistry via triboelectric charge. *J. Am. Chem. Soc*. https://doi.org/10.1021/jacs.4c09318 (2024).
41. Fan, F. R., Tang, W. & Wang, Z. L. Flexible nanogenerators for energy harvesting and self-powered electronics. *Adv. Mater.* **28**, 4283–4305 (2016).
42. Wang, Z. L. & Wang, A. C. On the origin of contact-electrification. *Mater. Today* **30**, 34–51 (2019).
43. Wang, Z. et al. Contact-electro-catalysis for the degradation of organic pollutants using pristine dielectric powders. *Nat. Commun.* **13**, 130 (2022).
44. Zhang, Z. et al. Efficient fluorocarbons capture using radical-containing covalent triazine frameworks. *J. Am. Chem. Soc.* **146**, 31213–31220 (2024).
45. Li, W. et al. Boosting reactive oxygen species generation via contact-electro-catalysis with Fe^{III}-initiated self-cycled Fenton system. *Angew. Chem. Int. Ed.* **64**, e202413246. (2024).
46. Zuo, S., Wang, Y., Wan, J. & Yi, J. Hydrogen bonding network in the electrical double layer mediates fast proton skipping to get rid of Fenton reaction pH dependence enables highly efficient alkaline water purification. *Water Res.* **268**, 122612 (2025).
47. Xiao, J., Guo, S., Wang, D. & An, Q. Fenton-like reaction: recent advances and new trends. *Chem. Eur. J.* **30**, e202304337. https://doi.org/10.1002/chem.202304337 (2024).
48. Wang, Z.-K. et al. Lewis acid-facilitated deep eutectic solvent (DES) pretreatment for producing high-purity and antioxidative lignin. *ACS Sustain. Chem. Eng.* **8**, 1050–1057 (2020).
49. Han, X. et al. A new strategy to strongly release sweet-enhancing volatiles from goji pomace using trivalent iron salts. *Food Res. Int.* https://doi.org/10.1016/j.foodres.2023.112659 (2023).
50. Marcotullio, G., Krisanti, E., Giuntoli, J. & de Jong, W. Selective production of hemicellulose-derived carbohydrates from wheat straw using dilute HCl or $FeCl_3$ solutions under mild conditions. X-ray and thermo-gravimetric analysis of the solid residues. *Bioresour* **102**, 5917–5923 (2011).
51. Motohashi, N. & Saito, Y. Competitive measurement of rate constants for hydroxyl radical reactions using radiolytic hydroxylation of benzoate. *Chem. Pharm. Bull.* **41**, 1842–1845 (1993).
52. Ma, D. et al. A green strategy from waste red mud to Fe^0-based biochar for sulfadiazine treatment by peroxydisulfate activation. *Chem. Eng. J.* **446**, 136944 (2022).
53. Wang, Z. et al. Aqueous iron(IV)-oxo complex: An emerging powerful reactive oxidant formed by iron(II)-based advanced oxidation processes for oxidative water treatment. *Environ. Sci. Technol.* **56**, 1492–1509 (2022).
54. Zhou, H. et al. Redox-active polymers as robust electron-shuttle co-catalysts for fast Fe^{3+}/Fe^{2+} circulation and green Fenton oxidation. *Environ. Sci. Technol.* **57**, 3334–3344 (2023).
55. Zhang, H., Zhang, D. B. & Zhou, J. Y. Removal of COD from landfill leachate by electro-Fenton method. *J. Hazard. Mater.* **135**, 106–111 (2006).
56. Sun, Y. & Pignatello, J. J. Photochemical reactions involved in the total mineralization of 2,4-D by iron(3+)/hydrogen peroxide/UV. *Environ. Sci. Technol.* **27**, 304–310 (1993).
57. Lee, J. K. et al. Spontaneous generation of hydrogen peroxide from aqueous microdroplets. *Proc. Natl Acad. Sci. USA* **116**, 19294–19298 (2019).

Acknowledgements

This work was supported by the National Natural Science Foundation of China [22476021 and 22476020], the National Key Research and Development Program of China [2022YFA0912503], the Natural Science Foundation of Guangdong [2025A1515010771], the Key Research Platforms and Projects of Guangdong Universities [2023ZDZX3038], and the Start-up fund for Postdoctoral of Dongguan University of Technology [221110168]. XPS data were obtained using equipment maintained by Dongguan University of Technology Analytical and Testing Center. The authors gratefully acknowledge the intellectual contributions from Prof. YH. Ao of Hohai University for insightful discussions on the mechanism.

Author contributions

D.M. and J.Z. contributed equally to this work. W.L.: Writing— review & editing, writing—original draft, supervision, funding acquisition, and conceptualization. J.M.: Writing—review & editing and formal analysis. K.H. and K.Y.: Methodology, investigation, and formal analysis. J.C.: Validation and formal analysis. Q.L.: Resources and formal analysis. M.Z. and F.C.: Resources and methodology. D.X.: Writing—review & editing, funding acquisition, and formal analysis. All authors reviewed the manuscript.

Competing interests

The authors declare no competing interests.

Additional information

Supplementary information The online version contains supplementary material available at https://doi.org/10.1038/s41545-025-00476-0.

Correspondence and requests for materials should be addressed to Wei Li.